UC Merced

UC Merced Previously Published Works

Title

Molecular Dynamics Simulation of the Stress–Strain Behavior of Polyamide Crystals

Permalink

https://escholarship.org/uc/item/6vh4519z

Journal

Macromolecules, 54(18)

ISSN

0024-9297

Authors

Yang, Quanpeng
Li, Wenjun
Stober, Spencer T
et al.

Publication Date

2021-09-28

DOI

10.1021/acs.macromol.1c00974

Peer reviewed

eScholarship.org Powered by the California Digital Library
University of California

Macromolecules 2021
10.1021/acs.macromol.1c00974

Molecular Dynamics Simulation of the Stress-strain Behavior of Polyamide Crystals

Quanpeng Yang,[†] Wenjun Li,[‡] Spencer T. Stober,[‡] Adam B. Burns,[‡] Manesh Gopinadhan,[‡] and Ashlie Martini[*,†]

[†]*Department of Mechanical Engineering, University of California-Merced, 5200 N. Lake Road, Merced, California 95343, United States*

[‡]*ExxonMobil Research and Engineering Company, 1545 Route 22 East, Annandale, New Jersey 08801, United States*

E-mail: amartini@ucmerced.edu

Abstract

Molecular dynamics simulations modeled the aramid poly(*p*-phenylene terephthalamide) (PPTA) and a related aromatic-aliphatic polyamide derived from a five-carbon aliphatic diacid (PAP5) with nine different reactive and non-reactive force fields. The force fields were evaluated based on crystal structures as well as intermolecular H-bonding and π-molecular interactions. The optimum force field was then used to simulate stress-strain behavior in the chain and transverse-to-chain directions. In the chain direction, PAP5 had higher ultimate stress and failure strain than PPTA; however, the stiffness of PAP5 was lower than PPTA at low strain (0-2%) while the reverse was observed at high strain (last 5% before failure). This contrast, and differences in the transverse direction properties, were explained by the methylene segments of PAP5 that confer conformational freedom, enabling accommodation of low strain without stretching covalent bonds. The simulation approach demonstrated here for two poly-

mers with distinct chemistry but similar atomic interactions may be extended to other polyamides.

Introduction

Hydrogen-bonded polymers are widely used in engineering applications due to their excellent mechanical and thermal properties.[1,2] Among the strongest hydrogen-bonded polymer fibers are aromatic polyamides (i.e., aramids). The most well-known example is poly(*p*-phenylene terephthalamide) (PPTA), which is also trademarked as Kevlar® and Twaron®. PPTA is used in flexible armor and other impact-resistant applications due to its excellent mechanical properties (superior strength-to-weight ratio and flexibility),[3] thermal stability (thermal decomposition temperature of 500° C),[4] and chemical resistance (to acid, alkali and organic solvent).[5–7] These superior mechanical and thermal properties originate from the structure of the PPTA fibers. X-ray diffraction (XRD) has shown[8] that PPTA fibers consist of a highly crystalline arrangement of extended PPTA chains aligned along the fiber axis with strong intermolecular hydrogen bonds (H-bonds), which govern chain packing and melting behavior.[1,9–11]

Although PPTA has many advantages, it has limitations as well. One main drawback is difficulty in processing because it is only soluble in highly aggressive polar solvents, such as concentrated sulfuric acid, making processing challenging and expensive.[12] Melt processing is intractable because of the inaccessible melting point of the material, so the primary route is currently solution processing. Regardless, it is desirable to design modified systems that improve processability without compromising other properties. To identify materials with properties comparable to PPTA (potentially with better processability), there has been increasing interest in understanding the effects of the structure and intermolecular forces within PPTA on its mechanical behavior.[5] Various experiments have been used to investigate these structure-property relationships for PPTA single fibers, including elastic loop,[13,14]

transverse compression,[15,16] axial tension[16] and torsion[16] tests. These measurements have been complemented by material and surface characterization tools including scanning electron microscopy, transmission electron microscopy[14] and XRD.[17] These studies revealed that crystallite orientation, rigidity of the molecular chains, defect density, and degree of molecular order are the main factors affecting the mechanical properties of PPTA.[14]

However, there are challenges associated with studying the mechanical properties of polymer crystals experimentally.[5] First, measurements on single fibers are difficult and time-consuming due to the micrometer length scale of the fibers, which necessitates both delicate handling and sensitive equipment.[18,19] Numerous measurements are also required to obtain reliable statistics given the unavoidable variability from sample to sample. In addition, experimental studies of the mechanical properties of PPTA in the directions transverse to the fiber axis focused only on compressive behavior[13–15] due to the difficulties associated with applying tensile strain in the transverse direction.[20] Finally, it is challenging to experimentally decouple the effects of fiber morphology (which is a product of processing) from the inherent molecular attributes.[21] Design of new materials requires insight into the relative contributions of intramolecular interactions and intermolecular interactions, i.e., hydrogen bonding (H-bonding) between amide groups and interactions between the π-manifolds of the aromatic rings (π-stacking or π-π stacking).[21]

Molecular dynamics (MD) simulations are a natural complement to experiments since they provide insight into material properties and behavior at the atomistic scale under controlled conditions.[5] MD simulations can help not only to interpret complicated experimental results, but also guide the development of new experimental methods. The ability of these simulations to accurately describe material properties depends on the empirical model force field for atomic interactions. There are two general types of force fields, reactive and non-reactive. With non-reactive force fields, bonds can be stretched and twisted but not be broken, while reactive force fields can capture the formation and breaking of chemical bonds. Previous simulations of PPTA have used both reactive and non-reactive force fields,

as discussed below.

The non-reactive Dreiding[22] force field was used to reproduce the molecular packing structure of PPTA polymer crystal.[23] Another non-reactive force field, COMPASS (Condensed-phase Optimized Molecular Potentials for Atomistic Simulation Studies),[24] was also used to study the properties of PPTA crystals.[10,25] One of those studies focused on the effects of microstructural and topological defects, such as chain ends, inorganic-solvent impurities, chain misalignment and sheet stacking faults on the strength, ductility and stiffness of PPTA crystals.[25] In another COMPASS simulation study,[10] the effect of torsion on the tensile properties of PPTA crystals was investigated.

PPTA has also been modeled using ReaxFF,[26] a reactive force field. The tensile response of PPTA crystals with defects was studied[27] using a ReaxFF parameter set developed by Budzien et al.[28] A ReaxFF parameter set developed by Liu et al.[29] was used to study the mechanical properties of PPTA in the presence of defects,[9] the influence of strain-rate and temperature on the mechanical strength,[30] and the effects of axial and transverse compression on the residual tensile stress of PPTA.[31]

These simulation-based studies have revealed important connections between intermolecular and intramolecular interactions and the material properties of PPTA. Simulations have shown that H-bonds form in the radial plane (parallel to the flat aromatic rings) and repeat along the chain axis forming "sheet-like" structures.[10,32] The interaction strength between adjacent PPTA chains is further increased by "inter-sheet" π-stacking.[10] This stacking mechanism contributes to the long-range, highly ordered structures observed in PPTA fibers.[33] Such simulations support the hypothesis that the excellent mechanical properties of PPTA fibers originate from the strong intermolecular interactions (H-bonding and π-stacking). In a study using ReaxFF, the effect of H-bonding on PPTA properties was quantified by numerically "turning off" the H-bond interactions in the force field, and a small decrease (1%) in tensile modulus was measured in the chain direction, but in the transverse directions, modulus and strength were reduced significantly (by 40% and 69%, respectively).[34]

The MD simulations of PPTA summarized above have used many different force fields to study various aspects of the material. One previous study compared two force fields (PCFF [35] and ReaxFF Liu[29]) for their ability to model PPTA structure and mechanical response to strain.[9] It was found that the PCFF and ReaxFF Liu force fields give similar results, except that PCFF can only be used for situations where primary bonds are not expected to rupture. However, there has been no direct comparison of a comprehensive set of force fields, including multiple reactive and non-reactive models. Further, since intermolecular interactions play an important role in the mechanical response of PPTA, force field comparisons should include evaluation of the ability to model H-bonding and π-stacking patterns. Finally, the accuracy of MD simulations is highly dependent on the suitability of the force field for the specific material system being studied, so generalizability must be assessed by evaluating homologous material systems.

Once an accurate force field and suitable methods have been identified, MD simulations can be used with confidence to investigate the effect of structural features that underlie the material properties of aromatic polyamides. For example, Deshmukh et al.[1] showed that the length of the methylene segments in aromatic-aliphatic polyamides affects the polymer conformation and structure. In their work, aromatic-aliphatic polyamides, prepared from *p*-phenylene diamine and aliphatic diacids, were referred to as PAPX, where X was the number of carbon atoms in the diacid monomer. They also showed that methylene units in PAP5 weakened the H-bonds and altered the topology of the H-bonding sheets relative to PPTA. However, the effect of these conformational differences between PPTA and PAP5 on mechanical properties was not explored.

To enable design of materials with mechanical properties comparable to PPTA, it is necessary to understand the relationships between polymer structure and mechanical behavior. Toward this goal, we used MD simulations to study the molecular scale mechanisms underlying the mechanical response of PPTA and PAP5. First, several force fields (both non-reactive and reactive) were compared to identify the most accurate model of the static

structures of PPTA and PAP5. This analysis included both unit cell lattice parameters as well as H-bonding and π-stacking distances. Different model sizes were also compared to identify the smallest possible system capable of accurately modeling these material properties. Then, using the reactive and non-reactive force fields that best captured the static structures of the materials, simulations were run to characterize the response of the polymer crystals to tension in the chain and transverse directions. Lastly, the optimum reactive force field was used to correlate the mechanical response of the materials to changes in H-bonding and π-stacking patterns, as well as how this behavior differed between PPTA and PAP5.

Methods

Structural Models

The polyamide models were initially constructed using Materials Studio,[36] with unit cell lattice parameters from X-ray diffraction[1] as listed in Table 1. The atomic positions were then adjusted manually in Materials Studio to match the model-predicted and experimental XRD patterns reported in Ref. 1. The initial density of PPTA was 1.50 g/cc, consistent with the experimentally measured densities in the range of 1.44-1.48 g/cc.[3,4] The chemical formulas and atomic-scale models of PPTA and PAP5 unit cells are shown in Fig. 1a and Fig. 1b, respectively. The chain direction was aligned with the x-axis, and the H-bonding and π-stacking directions were aligned with the y- and z-axes, respectively.

Table 1: Unit cell lattice parameters for PPTA and PAP5[1,37]

Polymer	a (Å)	b (Å)	c (Å)	α (°)	β (°)	γ (°)
PPTA	7.87	5.18	12.9	90	90	90
PAP5	8.50	4.70	24.8	90	85	90

The foundational element of the crystalline structure is the unit cell. PPTA and PAP5 have orthorhombic and monoclinic (pseudo-orthorhombic) crystal structures, respectively, but both[1,5,8,21,37] with two molecular chains per unit cell, one at the center and the other at

the corner of the cell viewed in the yz plane, see Fig. 1.[1,5,21,37] The main differences between their unit cell structures are: (1) PAP5 has four monomers in its c-axis repeat unit, whereas PPTA has only two; (2) the terephthalic acid monomer of PPTA is replaced by a diacid monomer with three methylene groups to form PAP5, so there are five carbon atoms and two -NH- groups between two adjacent aromatic rings in each PAP5 monomer, while there is only one carbon and one -NH- group between the two adjacent aromatic rings in each PPTA monomer; (3) the unit cell length c of PAP5 is almost twice that of PPTA (56 atoms in PPTA and 108 atoms in PAP5); and (4) there is a slight tilt of β in the unit cell of PAP5 while all lattice angles are 90° for PPTA.

After the unit cell was built, it was replicated by $N_x \times N_y \times N_z$ (1×1×1, 4×4×4, 6×4×4, 8×4×4, 6×6×6, and 8×8×8) in the x-, y- and z-directions to create simulation cells with a range of sizes. Note that the models with periodic boundary conditions in all three directions represent ideal crystalline polymers with infinite chain length and no defects or chain ends. This is an approximation of a physical crystalline polymer that will have finite length chains with defects and chain ends. However, the simulation methods developed here for an ideal crystal can be extended in future work to more realistic model structures.

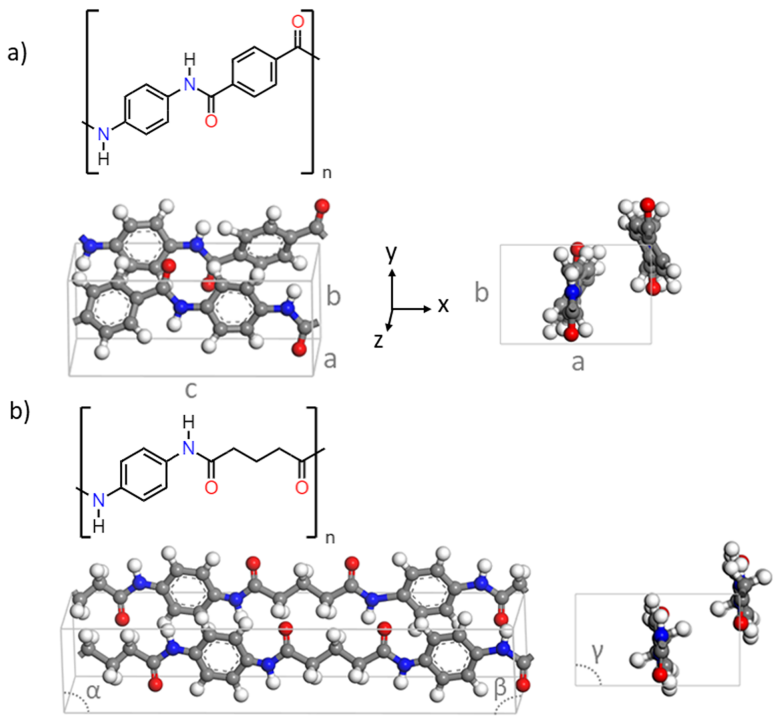

Figure 1: Unit cells of (a) PPTA and (b) PAP5 where lattice dimensions (a, b, and c) are identified on the PPTA snapshot and lattice angles (α, β, and γ) are identified on the PAP5 snapshot. The orthogonal directions (x, y, and z) are also defined with respect to the perspective views of the unit cells. Atom colors correspond to: oxygen, red; nitrogen, blue; carbon, gray; hydrogen, white. The cross-section views on the far right show the crystals from the yz plane.

Force Fields

Two non-reactive force fields were tested: OPLS (Optimized Potentials for Liquid Simulations)[38] and CVFF (Consistent Valence Force Field).[39] Seven different ReaxFF parameterizations were tested as well, chosen because they include all of the elements in our model systems (oxygen, nitrogen, carbon, and hydrogen). Each ReaxFF parameter set is referred to subsequently by the last name of the first author of the paper in which it was first reported, including Zhang,[40] Budzien,[28] Kamat,[41] Mattsson,[42] Wood,[43] Liu[29] and Vashisth.[44] Each of these was parameterized for different molecular systems, as summarized in Table 2.

Table 2: ReaxFF parameter sets and the molecular systems for which they were first parameterized are identified by the last name of the first author of the corresponding paper in order of publication date.

Force Field	Material System for Parameterization
Zhang (2009)[40]	Thermal decomposition of hydrazines
Budzien (2009)[28]	Thermomechanical properties of pentaerythritol tetranitrate
Kamat (2010)[41]	Laser-induced incandescence of soot
Mattsson (2010)[42]	Polyethylene and poly(4-methyl-1-pentene)
Wood (2014)[43]	Decomposition of the high-energy-density material α-HMX
Liu (2014)[29]	Polyethylene and energetic materials
Vashisth (2018)[44]	Cross-linking of polymers

Simulation Protocol

All of the MD simulations in this study were carried out using an open source MD simulation package LAMMPS (Large-scale Atomic/Molecular Massively Parallel Simulator).[45] Software OVITO (Open Visualization Tool)[46] was used for model visualization. The MD time step was 0.25 fs for all simulations. Temperature and pressure were controlled using a Nosé-Hoover thermostat[47] and barostat[48] with damping parameters of 25 fs and 250 fs, respectively. The cut-off distance for Lennard-Jones and electrostatic interactions was 1.5 nm for non-reactive force fields. For the ReaxFF force fields the default cut-offs were used (in LAMMPS, nbrhood_cutoff was 0.5 nm and hbond_cutoff was 0.75 nm). First, the replicated simulation cell was energy minimized. Then, simulations were run in the NPT (constant number of atoms, pressure and temperature) ensemble for 125 ps (until the lattice parameters reached steady-state) at 300 K and 1 atm. The dimensions of the simulation cell were averaged after steady-state was reached, i.e., over the last 12.5 ps (50 frames) of the NPT simulation, to calculate the system lattice parameters.

For a subset of the force fields, simulations were run to calculate stress-strain behavior, following the method developed in our previous work for crystalline cellulose.[49] After equilibrating the simulation cell in the NPT ensemble, the system was stretched in one direction (x-, y-, or z-direction) through successive small steps (0.25% strain). After applied deforma-

tion, the simulation cell was equilibrated in an NPT ensemble with the stretching direction fixed and the perpendicular directions relaxed for 2.5, 0.25 or 0.025 ps. The relaxation time was determined by the strain step increment (0.25%) divided by the prescribed strain rate. Therefore, the relaxation times modeled here corresponded to overall strain rates of 1×10^{9}, 1×10^{10} or 1×10^{11} s^{-1}. This process was repeated until the total strain reached 25%. The step-wise strain method has been used in previous studies[49–53] to minimize unphysical mechanical response that may arise due to insufficient time for the atoms to respond to rapid changes in the system size at high strain rates. Note that we also tested a continuous strain rate approach[54] and the results were almost the same (Fig. S1).

The stress values at each strain increment were calculated by averaging over the last 10% of the equilibration with that strain increment applied. The same procedure was performed in the three orthogonal directions, x (chain), y (H-bonding) and z (π-stacking). The bulk mechanical properties were then estimated from the resultant stress-strain curves. The elastic modulus was calculated by applying a linear fit to the stress-strain data from 0-2% strain. This calculation was performed over different ranges of strain, as discussed later. The failure strain was the strain where the first polymer chain breaks (the sharp drop of stress-strain curve), which is only possible for the reactive potentials. The ultimate stress was taken from the stress at failure strain. These simulations were repeated three times independently with different random velocity seeds assigned for the atoms in the initial structure before NPT simulation.

Results and Discussion

Force Field Evaluation

Lattice Parameters

The average value of each lattice parameter (a, b, c, α, β, γ) for the 4×4×4 models of PPTA and PAP5 was determined for each force field. The error was then calculated from the difference between the average lattice parameters in our MD simulation and those reported in the literature measured from XRD reported in Ref. 1. $Error = \left| \frac{1}{N} \sum l_{MD} - l_{XRD} \right|$, where l is one of the lattice parameters and N is the number of simulation frames averaged. The error for the six lattice parameters for all force fields tested is summarized in Fig. 2.

The error analysis shows that most of the force fields tested were able to reproduce the lattice parameters of PPTA with reasonable accuracy (less than 25% cumulative error). For both PPTA and PAP5, with many of the force fields, the largest error was for the a parameter. This is likely due to the limitations of those force fields to accurately capture π-stacking. The exceptions were Liu (largest error for PPTA was α), Wood (largest error for PAP5 was γ), CVFF and OPLS (largest error for PPTA was b and for PAP5 was γ). Also, for most of the force fields, the error was larger for PAP5 than PPTA. Based on this analysis, the Kamat, Liu, Vashisth and OPLS force fields were identified as the most accurate in terms of both PPTA and PAP5 lattice parameters.

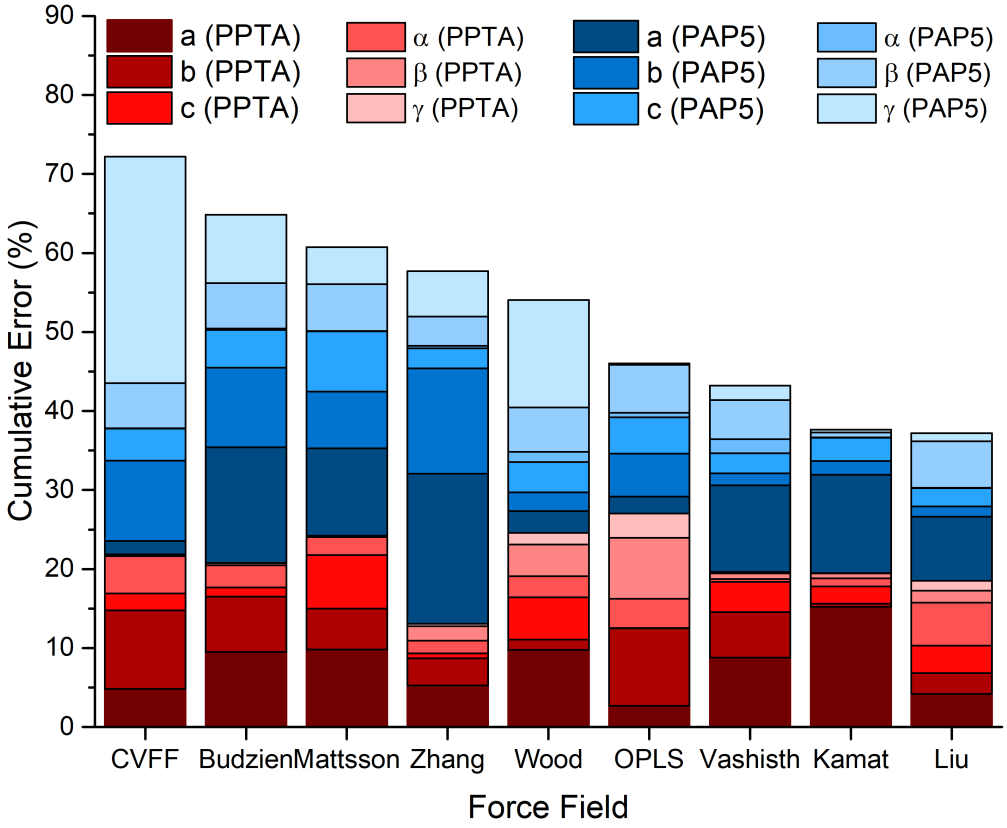

Figure 2: Comparison of the cumulative error in the lattice parameters for PPTA and PAP5 of seven reactive and two non-reactive force fields.

H-bonding and π-stacking

Since H-bonding and π-stacking have been found to play important roles in the mechanical properties of polyamides,[1,9–11] an appropriate force field should be able to capture these non-bonded interactions accurately. To test this, the radial distribution functions (RDFs) of interatomic distances were calculated for all force fields, except CVFF, which exhibited the least accurate lattice parameters, and was excluded from subsequent analysis. OPLS is the sole non-reactive force field considered henceforth. H-bond length was quantified from RDFs of the non-bonded, nearest-neighbor N–O distance. This definition is widely used [1,9] because the position of the H atom in N-H···O is difficult to determine experimentally. The reference N–O distances for PPTA and PAP5 were reported to be 3.0 and 2.9 Å in Ref. 1 and 8, calculated from experiments and simulations. The reference N-H···O angle (H-bond angle)

for PPTA was reported to be 160°,[8] which is consistent with our results for PPTA (158°) and PAP5 (161°) after equilibrium. Although H-bond strength is determined by both distance and angle, here we primarily use the N–O distance to quantify H-bonding. π-stacking was measured as the distance in the z-direction (π-stacking-direction) between the centers of two adjacent aromatic rings. The reference value is 3.9 Å for both PPTA and PAP5.[1]

The H-bonding RDFs (N–O distance) calculated for PPTA and PAP5 with each force field are shown in Fig. 3. The reference values are identified by vertical dashed lines. The accuracy of the force fields is evaluated by comparing the reference distance to the position of the peak of the RDF. For PPTA, the Wood force field is reasonably accurate, albeit with a wide peak, indicating more variation in atom-atom distances within the model system, i.e., the effect of cumulative error. Also, Budzien and Mattsson slightly overpredict the H-bond distance while Zhang, Vashisth and Liu slightly underpredict it. There is a similar trend in the force fields for PAP5. Based on qualitative analysis of the position of the RDF peaks (closer to the reference value is more accurate) and width of the peak (narrower peaks correspond to less variation from bond-to-bond within the polymers), the best force fields in terms of H-bonding for PAP5 are OPLS, Wood, Zhang, Vashisth and Liu.

The RDFs for π-stacking in PPTA and PAP5 are shown in Fig. 4. The force fields are again evaluated based on the position and width of RDF peaks. Note that the position of the π-stacking RDF peak also reflects the accuracy of the lattice parameter a. As such, force fields that underpredicted the π-π stacking distance also had large error in their prediction of a (see Fig. 2). For PPTA, the RDF peaks of Liu and OPLS are the closest to the reference value. For PAP5, Wood and Liu are the most accurate, with relatively narrow peaks.

Based on the evaluation of the various force fields in terms of their ability to accurately reproduce the unit cell lattice parameters and preferred H-bonding and π-stacking distances, the Liu or Vashisth parameter sets within the ReaxFF formalism performed best. Therefore, the Liu and Vashisth ReaxFF force fields were selected for the stress-strain simulations, discussed below. Stress-strain simulations were also performed with the commonly employed,

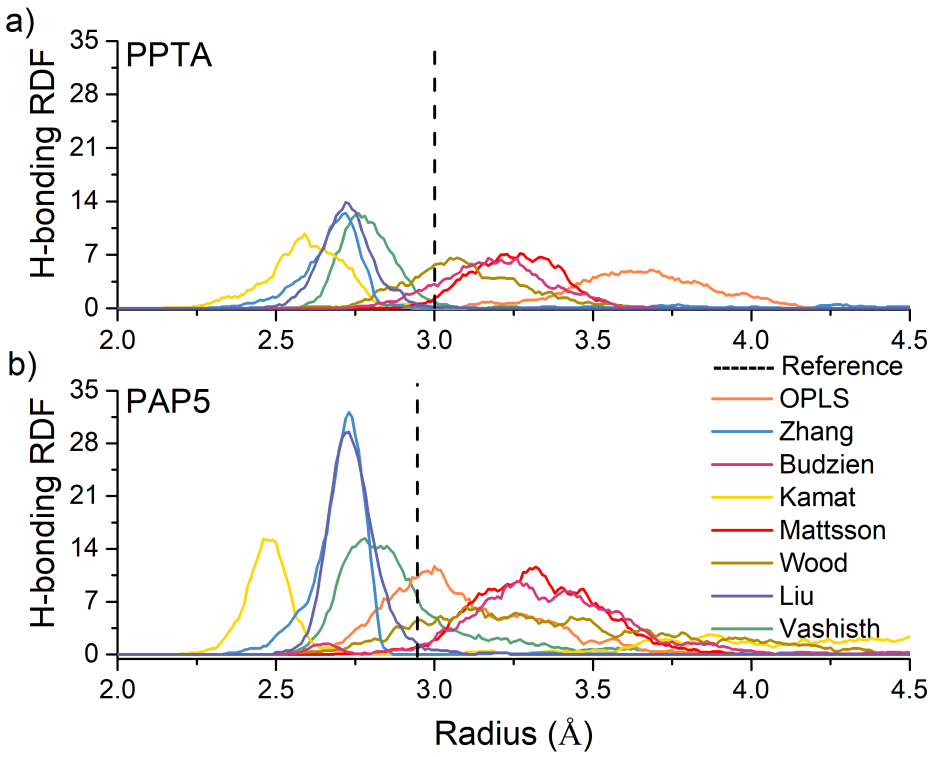

Figure 3: Comparison of H-bonding (non-bonded, nearest-neighbor N–O) radial distribution functions calculated for (a) PAP5 and (b) PPTA. The reference[1] H-bond lengths (N–O distances) for PPTA and PAP5 are shown as vertical dashed lines.

non-reactive OPLS force field for comparison.

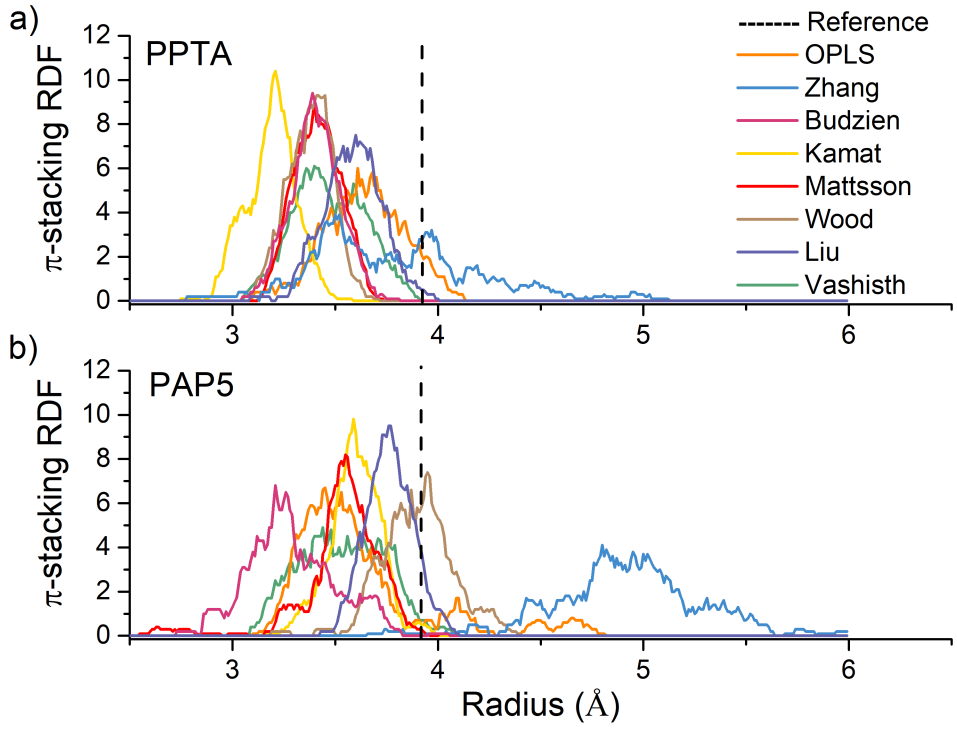

Figure 4: Comparison of π-stacking radial distribution functions calculated for (a) PAP5 and (b) PPTA. The reference π-stacking distances[1] are shown as vertical dashed lines.

Stress-Strain Behavior

First, it is necessary to determine the appropriate system size for these simulations to minimize finite size effects while maintaining computational efficiency. The goal is to identify the smallest model that can be used (to maximize computational efficiency) without simulation artifact that may occur if the model is too small due to the unphysical topology of the simulation, e.g., if the model system is too small, a molecule may interact with its own image across the periodic boundary. The stress-strain simulations were run for PPTA with system sizes ranging from 1×1×1 to 8×8×8 with strain applied in the x-, y- and z-directions at a strain rate of 1×10^{9} s^{-1}.

The results for the OPLS, Liu and Vashisth force fields are shown in Fig. 5. It can be seen that, for the Liu and Vashisth force fields, the curves start to converge at $4 \times 4 \times 4$, which suggests that a system size of $4 \times 4 \times 4$ is big enough to minimize finite size effects

(this size model was also used in previous mechanical studies of cellulose nanocrystals[49]). However, for OPLS, although the stress-strain curves in the x-direction start to converge at $1 \times 1 \times 1$, there is no obvious convergence in the data with increasing system size for strain in the y- and z-directions. The sharp drop in stress for some OPLS systems is due to the sudden occurrence of inter-chain slip (Fig. S2). The fluctuations in the stress-strain curve for some Vashisth systems in the z-direction starting is due to the occurrence of chain buckling (Fig. S3). Regardless, this analysis indicates that a minimum size of $4 \times 4 \times 4$ should be reliable for stress-strain simulations.

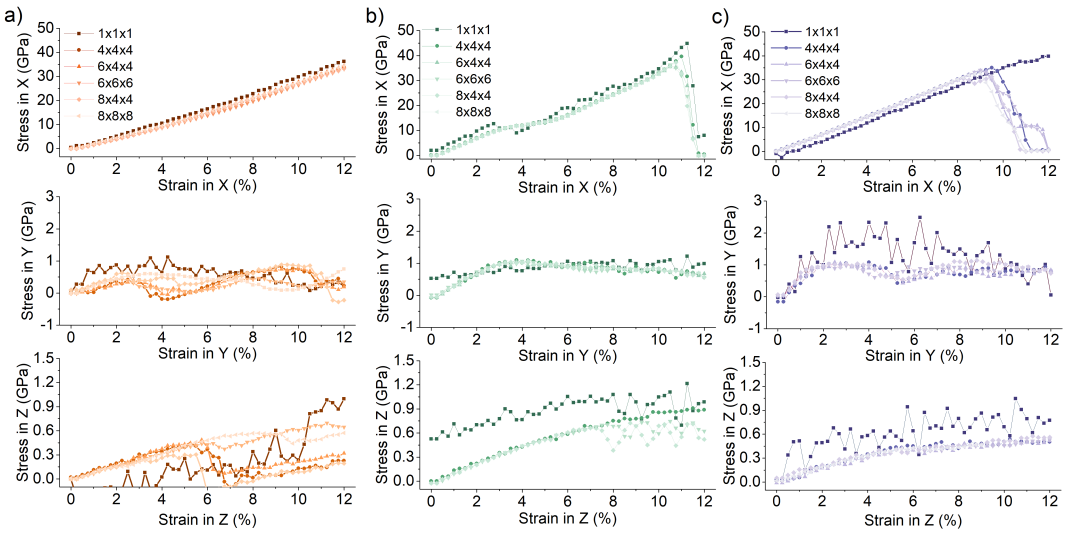

Figure 5: Evaluation of the stress-strain curves with the (a) OPLS, (b) ReaxFF Vashisth and (c) ReaxFF Liu force fields for PPTA with simulation box sizes between $1 \times 1 \times 1$ and $8 \times 8 \times 8$ in x-, y- and z-directions.

One obvious difference between the reactive (Liu and Vashisth) and non-reactive (OPLS) force fields is that, in the simulation of strain in the x-direction (chain-direction) the stress drops after $\sim$10% strain with the reactive force fields, but not with OPLS. This is because non-reactive force fields cannot capture breaking covalent bonds.[55] Therefore it is not possible to model ultimate properties using OPLS force field, particularly for strain in the polymer chain direction where material failure must occur through breaking of covalent bonds.

In contrast, ReaxFF utilizes a bond order approach to describe the chemical bonds. Also, ReaxFF models H-bonding with a specific energy functional term,[26,55,56] which is particularly

important for capturing weak H-bonding that is quite common in organic systems. Therefore, using ReaxFF, it is possible to study crystallite failure mechanisms involving primary (covalent) and/or secondary (hydrogen) bond rupture.[9] This indicates that a reactive force field should be used to analyze the mechanical properties of PPTA and PAP5.[5]

Comparing the Liu and Vashisth force fields in Fig. 5, the stress-strain trends in the y-direction are similar. However, there are fluctuations in the stress response to strain in the z-direction with some of the larger box sizes with the Vashisth force field, whereas all results with the Liu are quite stable. Recall also that the cumulative error of lattice parameters in Fig. 2 was lowest for the Liu force field. Therefore, the $4 \times 4 \times 4$ model and the ReaxFF Liu force field were used in the subsequent investigation of the stress-strain response of PPTA and PAP5.

Structure-Property Relationship

Mechanical Properties

Fig. 6 shows the mechanical properties (elastic modulus, ultimate stress, and failure strain) of PPTA and PAP5 calculated from simulations of strain in the x-direction (chain-direction) run at three different strain rates (1×10^{9}, 1×10^{10} and 1×10^{11} s^{-1}) with the ReaxFF Liu force field. For PPTA, the values obtained from simulations are compared to properties reported from previous experimental studies.[11,14,19,57,58] In general, the magnitude of strain-rate-dependent mechanical properties can appear larger when computed by molecular simulation. This is because the inherently small time scales accessible by molecular simulation lead to very high strain rates (typically $> 10^{8}$ s^{-1}).[3,33,59,60] For example, it was reported that chain direction mechanical properties of PPTA increase with strain rate,[3,30,59,61,62] consistent with the results in Fig. 6. This strain-rate-dependence has been attributed to the intermolecular slippage and plastic flow that occurs at low strain rates, resulting in more energy dissipation.[5] In addition, our model systems are infinite chain-length and free of defects (e.g., chain ends, stacking faults, or impurities), in contrast to physical materials. It has been reported that chain

end defects and different defect distribution patterns could reduce the ultimate stress and failure strain, and that the axial modulus increases with increasing chain length.[9] Moreover, in higher order structures such as fibrils, where the morphology is more complicated, chain and/or crystal misorientation might affect material properties. For all these reasons, the simulation-predicted mechanical properties are higher than values obtained from physical experiments.

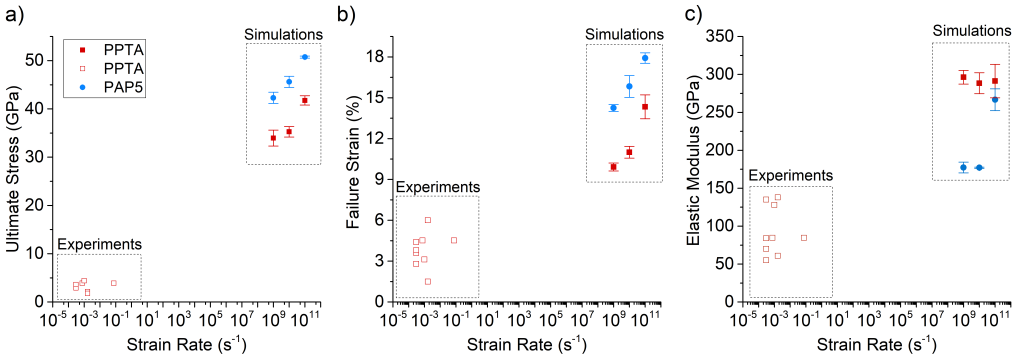

Figure 6: (a) Ultimate stress, (b) failure strain and (c) elastic modulus (calculated from 0 to 2% strain) from simulations of PPTA and PAP5 strained in the chain direction at three different strain rates (1×10^{9}, 1×10^{10} and 1×10^{11} s^{-1}) using the ReaxFF Liu force field. The error bars reflect the standard deviation calculated from three independent simulations. Also shown are representative data points for PPTA from experiments.[11,14,19,57,58]

Although we do not have experimental data for PAP5, the simulations enable comparison of PPTA and PAP5 at high strain rates. Like PPTA, the magnitudes of the ultimate stress and failure strain increase with increasing strain rate. However, at any strain rate, PAP5 has larger failure strain and ultimate stress than PPTA, but a smaller elastic modulus. Although the OPLS potential cannot simulate mechanical failure due to bond breakage, it was used to calculate elastic modulus and showed higher stiffness for PPTA than PAP5 (223±8 GPa for PPTA and 120±3 GPa for PAP5), confirming the direction and relative magnitude of the trend observed from ReaxFF. These results indicate that the methylene units in the PAP5 reduce stiffness but increase the failure strain. However, as discussed later, the elastic response of PAP5 is strain dependent, so the stiffness calculation depends on the strain range for which the linear fit is performed. These trends are investigated next.

Chain Direction Strain Response

Figs. 7a-b show the stress-strain behavior of PPTA and PAP5 for strain up to 25% in the x-direction at a strain rate of 1×10^9 s^{-1}. The corresponding mechanical properties are summarized in Table 3. The mechanical properties of PPTA predicted by our simulations are similar to the range of results reported in previous MD simulation studies with ReaxFF: elastic modulus 325-360 GPa, ultimate stress 32-35 GPa, and failure strain ∼10%.[9,27,34,63]

Table 3: Mechanical properties calculated from simulations of strain in the x-direction. For the elastic modulus, low-strain refers to 0-2% strain, high-strain refers to the last 5% strain prior to failure, and all-strain refers to all strain prior to failure. The errors are the standard deviation calculated over three independent repeat simulations.

Properties in the x-direction	PPTA	PAP5
All-strain modulus (GPa)	362±9	310±3
Low-strain modulus (GPa)	293±18	174±3
High-strain modulus (GPa)	375±5	436±10
Failure strain (%)	9.9±0.3	14.3±0.3
Ultimate stress (GPa)	34.0±1.6	42.3±1.1

Consistent with Fig. 6, failure stress and strain are larger for PAP5 than PPTA. However, the elastic modulus comparison is more complicated. The stress-strain curve for PPTA (Fig. 7a) has only one linear regime from zero strain to its failure strain at ∼10%. In contrast, the stress-strain curve for PAP5 (Fig. 7b) can be separated into two linear regimes: low-strain (0 to ∼4%) and high-strain (∼5 to ∼14%). Analysis of the lattice parameters during strain showed that γ increased sharply at this inflection point, indicating a structural transition, specifically, a contraction in the cross-sectional area (yz plane). This contraction also resulted in a strengthening of the H-bonding, quantified by a small decrease of the average H-bond length from 2.82 Å before the transition to 2.75 Å after the transition. The inflection point between these two regimes does not indicate yield, as confirmed by simulations in which the system was strained to 7.5% and then allowed to relax in the NPT ensemble at 300 K and 1 atm without constraints. When the constraint was released, the stress dropped to zero and the lattice parameters returned to their original pre-strain values

in approximately 10 ps (Fig. S4). This indicates that the deformation is elastic and PAP5 crystals exhibit two linear elastic regimes before failure. If the two elastic regimes in Fig. 7b are considered separately, the low-strain modulus is 174 GPa and the high-strain value is 436 GPa. Although PPTA exhibits some strain hardening, there is no sharp inflection point and the increase of modulus with strain is much lower than that observed for PAP5. As a result, the modulus of PAP5 is smaller than that of PPTA at low strain but the opposite is observed at high strain.

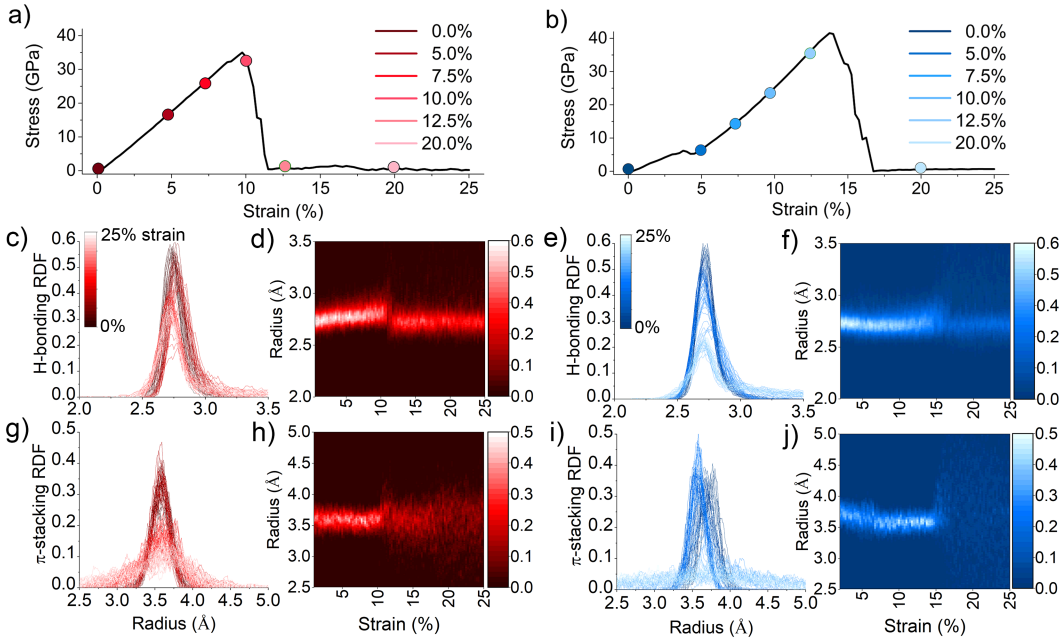

Figure 7: Stress-strain behavior (a and b) and RDF profiles and heat maps for H-bonding (c, d, e, and f) and π-stacking (g, h, i, and j) for PPTA (c, d, g, and h) and PAP5 (e, f, i, and j) strained in the x-direction. The RDFs are normalized by the number of bonds per unit cell. Movies showing the evolution of the stress and RDF distributions as well as the time evolution of the models are available in the Supplemental Information.

The RDFs for intermolecular H-bonding and π-stacking within PAP5 and PPTA at different strains are shown in Figs. 7c-j. The H-bonding RDF peak of PPTA (Figs. 7c-d) shifts to larger radii as the chains are being strained. However, the H-bonding RDF peak of PAP5 (Figs. 7e-f) first shifts to smaller radii at low strains then shifts to larger radii at higher strains. Regarding the π-stacking RDFs, for PPTA, the peak position changes very little with strain, but the peak widens. For PAP5, the π-stacking RDF first shifts to the left

at low strains and then becomes narrower as it is strained.

Snapshots from the simulations of PPTA and PAP5 at the strains identified in Fig. 7 are shown in Fig. 8. The snapshots show that both PPTA and PAP5 respond elastically at low strain followed by chain breaking at high strain. However, there are differences between PAP5 and PPTA observed as well. Specifically, it can be seen that, at zero strain, the PPTA is fully extended and then the chains are stretched as strain is applied. In contrast, the PAP5 chains have a wavy structure at zero strain. The waves are removed by extension at low strain and then the covalent bonds themselves begin to stretch at larger strain.

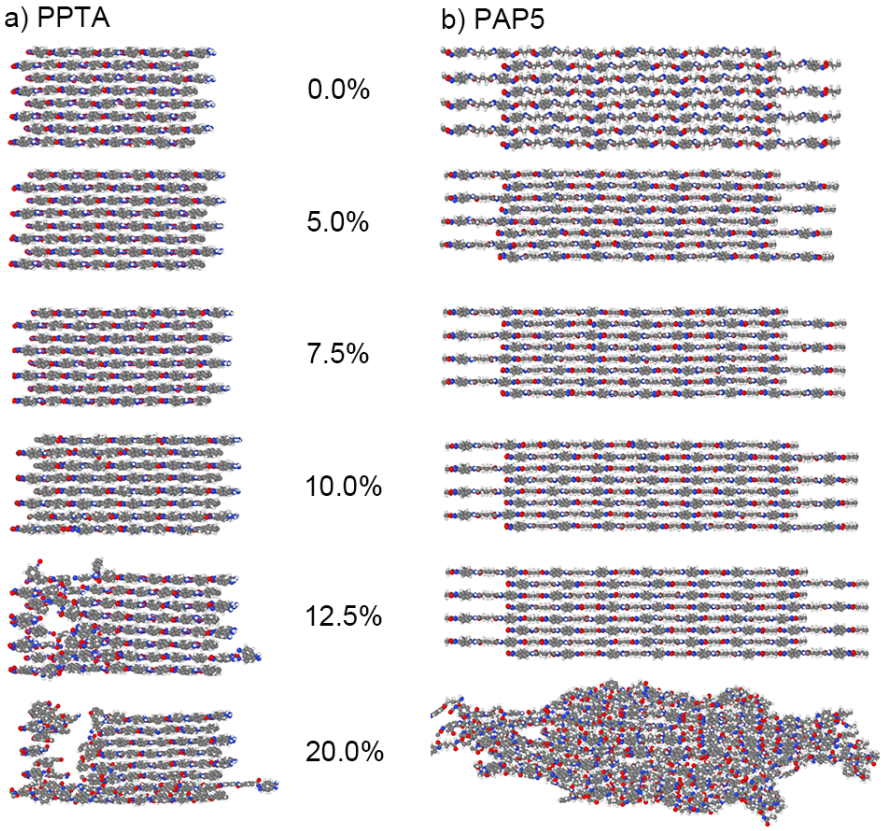

Figure 8: Snapshots of (a) PPTA and (b) PAP5 while strained in x-direction with a strain rate of 1×10^{9} s^{-1} at 0, 5, 7.5, 10, 12.5 and 20% strains with the Liu force field as viewed from the y-direction. Snapshots correspond to the solid circles on the stress-strain plots in Fig. 7.

The conformations of PPTA and PAP5 reflect two polymer conformations commonly reported in the literature:[21,64–77] extended and wavy. Note that a variety of different terms

have been used to describe these two conformation in the literature, but here the terms extended and wavy will be used. A wavy conformation is due to the methylene groups acting as spacers between the hydrogen-bonded amide groups, which increases the conformational freedom of the polymer chains.[1,78] A previous investigation of twenty-five different polymers (including polyethylene (PE) and poly tetrafluoroethylene (PTFE)) revealed that, at low strain, the polymer conformations are closely related to the force required to stretch them.[64]

It has been shown that polymers with a loose wavy conformation exhibit a much lower stiffness than polymers with extended conformations because extended conformations have stronger H-bonds between adjacent chains.[64–66] Another study examined the relationship between the elastic modulus, molecular conformation and flexibility of the chains of PPTA and related polymers.[21] They found that PPTA chains are fully extended, resulting in a high elastic modulus. The same study compared the extended and wavy forms of polyethylene oxybenzoate (PEOB) and found that the former had a much higher elastic modulus due to its extended conformation.[21]

To quantify waviness and its evolution with strain, we identified the positions of the backbone atoms in each chain in the yz plane. This analysis excluded the H and O atoms, and the C atoms in the aromatic rings. The results are shown in Fig. 9. In this figure, all the chains in the crystal are aligned by relocating their centroid to the origin of the yz plane at each strain.

At zero strain, the size and shape of the distributions of atoms in PPTA and PAP5 are different. The PPTA atoms fall into two, relatively small circular regions ($|y| < 1$ Å and $|z| < 0.75$ Å). In contrast, the PAP5 atom distribution is much more spread out ($|y| < 0.75$ Å and $|z| < 1.25$ Å), showing that the atoms are further from the chain axis, i.e., exhibiting a wavy conformation. The PAP5 atom distribution is also asymmetric, indicating there is some rotation of methylene units in the yz plane; this is not observed for the PPTA.

Once strain is applied, the size and shape of the atom distribution for the PPTA changes little, consistent with its extended conformation which accommodates strain by stretching

covalent bonds. However, the distribution of atoms in PAP5 becomes smaller and more symmetric with increasing strain. This indicates that strain is initially accommodated by elongation and rotation of the wavy chains.

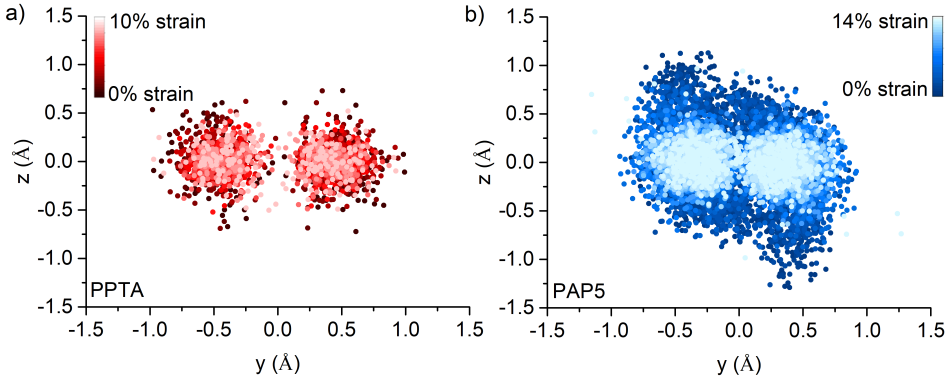

Figure 9: Position of atoms in the chains projected on the yz plane for (a) PPTA and (b) PAP5, where the centroid of each chain is manually moved to the origin of the yz plane. The hydrogen and oxygen atoms, and the carbon atoms in aromatic rings are excluded in this calculation.

The initial waviness of the PAP5 explains its smaller low-strain stiffness since less force is needed to elongate and rotate the methylene segments in PAP5 than to strain the covalent bonds within the extended chains of PPTA. This can be confirmed by the H-bonding and π-stacking RDFs in Figs. 7c-j. The H-bonding RDF peak position for PAP5 moves to the left (indicating stronger intermolecular interactions due to more ordered chains) with increasing strain as the waviness is removed. In contrast, for PPTA, the H-bonding peak position moves to the right and broadens (indicating weaker intermolecular interactions due to the loss of H-bond registry) as the covalent bonds within the chains are strained. A similar trend can be found in the π-stacking RDFs at low strain in Figs. 7g-j, where the peak for PAP5 shifts to the left and becomes narrower (strengthening π-stacking interactions) as the wavy chains are extended.

The difference between the initial conformations of PAP5 and PPTA also explains the larger failure strain of PAP5 than PPTA. Specifically, the larger failure strain is due to the initial waviness of PAP5, which enables it to accommodate the initial strain by extension of

the wavy chains such that stretching of covalent bonds does not begin until higher strains.

After the initial 5% strain, the conformations of PPTA and PAP5 are similar. Therefore, differences in their high-strain stiffness and ultimate stress, both of which are larger for PAP5 than PPTA, cannot be directly explained by the waviness argument. It has been reported that amide bonds contribute significantly to the chain direction elastic modulus of materials such as cellulose and polyamides.[79,80] Also, the amide group C-N bond has been identified as the weakest bond in the polymer chain backbone of PPTA,[9] consistent with the observation that failure of both PPTA and PAP5 in the chain direction occurred through breaking of the C-N bond. Therefore, C-N bond is expected to be the limiting factor of the overall strength of PPTA and PAP5. The average C-N bond length in PPTA is 1.44 Å and is 1.43 Å for PAP5 at failure strain, suggesting that the C-N bonds in PAP5 may be slightly stronger than those in PPTA.

A higher degree of chain alignment (less conformational freedom) is known to increase tensile strength and elastic modulus in polymers[80] and the high degree of alignment of PPTA has been attributed to intermolecular H-bonding.[9,11,15,81,82] From the analysis of the coplanarity of aromatic rings in the PPTA and PAP5 crystals at each strain (Fig. S5), it can be seen that, before failure, the ring-ring angle increased slightly (less aligned) with strain in PPTA but decreased (more aligned) in PAP5 as the chains transitioned from wavy to extended before plateauing in the high-strain regime. This phenomenon contributes to the sharp increase in the modulus of PAP5 in the high-strain regime.

Response to Strain in the Transverse Directions

The mechanical properties of PPTA and PAP5 exhibit anisotropy, as shown in Fig. 5. The elastic modulus and ultimate stress in the x-direction (chain-direction) are expected to be much higher than those in transverse directions since intramolecular covalent bonds resist strain in the x-direction but do not contribute to material properties in the y- and z-directions (directions aligned with H-bonding and π-stacking, respectively). Such anisotropy in me-

chanical properties has been reported for many other high-performance fibers[83] and explained by the high degree of chain orientation in the axial direction.[4] The mechanical properties of PPTA and PAP5 calculated from simulations of strain in the transverse directions are summarized in Table 4. The elastic modulus of PPTA in the transverse directions were calculated to be 8 GPa and 60 GPa in the y and z directions, respectively, consistent with the range of 4.1-52 GPa reported in a previous study.[63]

Table 4: Mechanical properties calculated from simulations of strain in the y- and z-directions.

Properties	PPTA	PAP5
y-direction		
Elastic modulus (GPa)	60	26
Yield strain (%)	3.0	6.5
Yield stress (GPa)	1.21	1.55
Failure strain (%)	24.3	24.8
Ultimate stress (GPa)	1.31	0.90
z-direction		
Elastic modulus (GPa)	8.4	13.2
Yield strain (%)	∼5.5	∼6.2
Yield stress (GPa)	∼0.43	∼0.68
Failure strain (%)	25	19
Ultimate stress (GPa)	0.72	0.99

The stress-strain curves and RDFs for strain in the y-direction are shown in Fig. 10, with corresponding snapshots in Fig. 11. Strain in the y-direction is primarily accommodated by the H-bonds between the chains. Therefore, as the crystal is strained, the peak of the H-bonding RDFs decreases in height and shifts to the right in Figs. 10c-f, indicating weakening and then breaking of H-bonds. The π-stacking RDF peak shifts to the left with increasing strain, as shown in Figs. 10g-j. This reflects Poisson contraction in the z-direction.

In the y-direction, both the Young's modulus and ultimate stress are larger for PPTA than for PAP5. PPTA has stronger H-bonding than PAP5 due to the more favorable chain conformations of PPTA; this conclusion is also supported by the experimental work of Deshmukh et al.[1] Since y-direction strain is in the direction of the H-bonding, the higher stiffness

and strength of PPTA are directly attributable to its stronger intermolecular H-bonding.

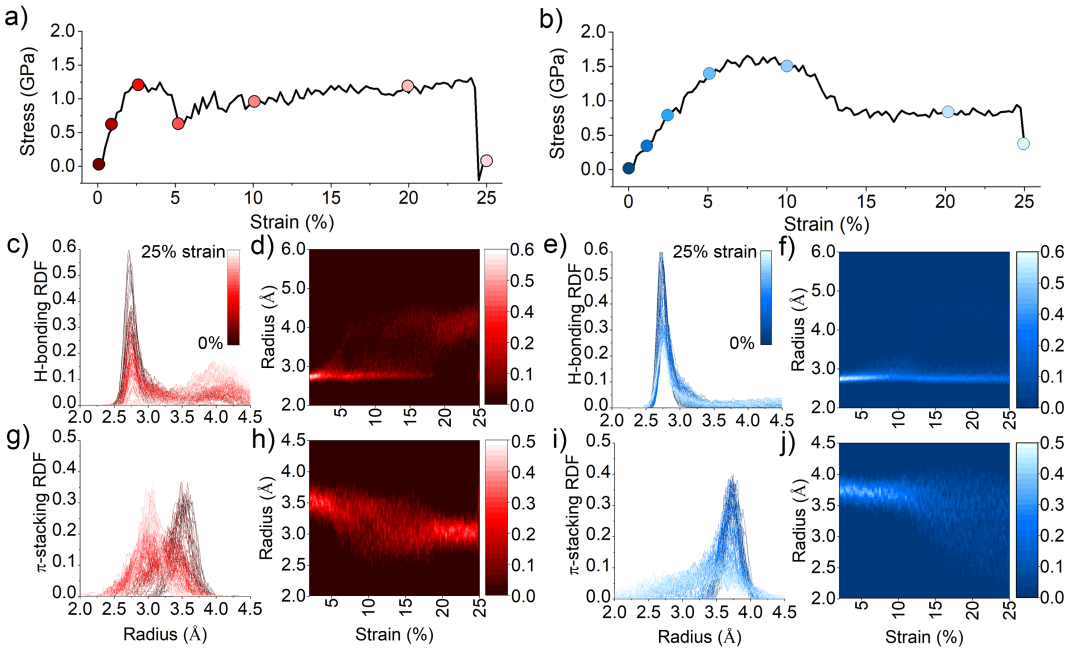

Figure 10: Stress-strain behavior (a and b) and RDF profiles and heat maps for H-bonding (c, d, e, and f) and π-stacking (g, h, i, and j) for PPTA (a, c, d, g, and h) and PAP5 (b, e, f, i and j) strained in the y-direction. The RDFs are normalized by the number of bonds per unit cell. Movies showing the evolution of the stress and RDF distributions as well as the time evolution of the models are available in the Supplemental Information.

Unlike the x-direction behavior, the crystals exhibited a yield point when strained in the y-direction. Yield occurred at a higher strain and larger stress for PAP5 compared to PPTA, so this trend could not be explained by H-bonding. However, analysis of the deformation (see movies in Supplemental Information) indicated that yield occurred through different mechanisms for these two polymers. For PAP5, yield occurred through breaking of its relatively weaker H-bonds while, for PPTA, the strong H-bonds resisted breaking and, instead, inter-sheet slip occurred at the yield point (see Supplemental Information Fig. S6). Inter-sheet slip resulted in a step-change reduction in the ring-ring angle, which brings the pi-pi stacking into better registry. No such mechanism is active in PAP5, which instead yields by H-bond breaking. Hence, the stress at which slip occurs in PPTA is lower than the stress for H-bond breaking in PAP5.

The stress-strain response and RDFs for strain in the z-direction are shown in Fig. 12,

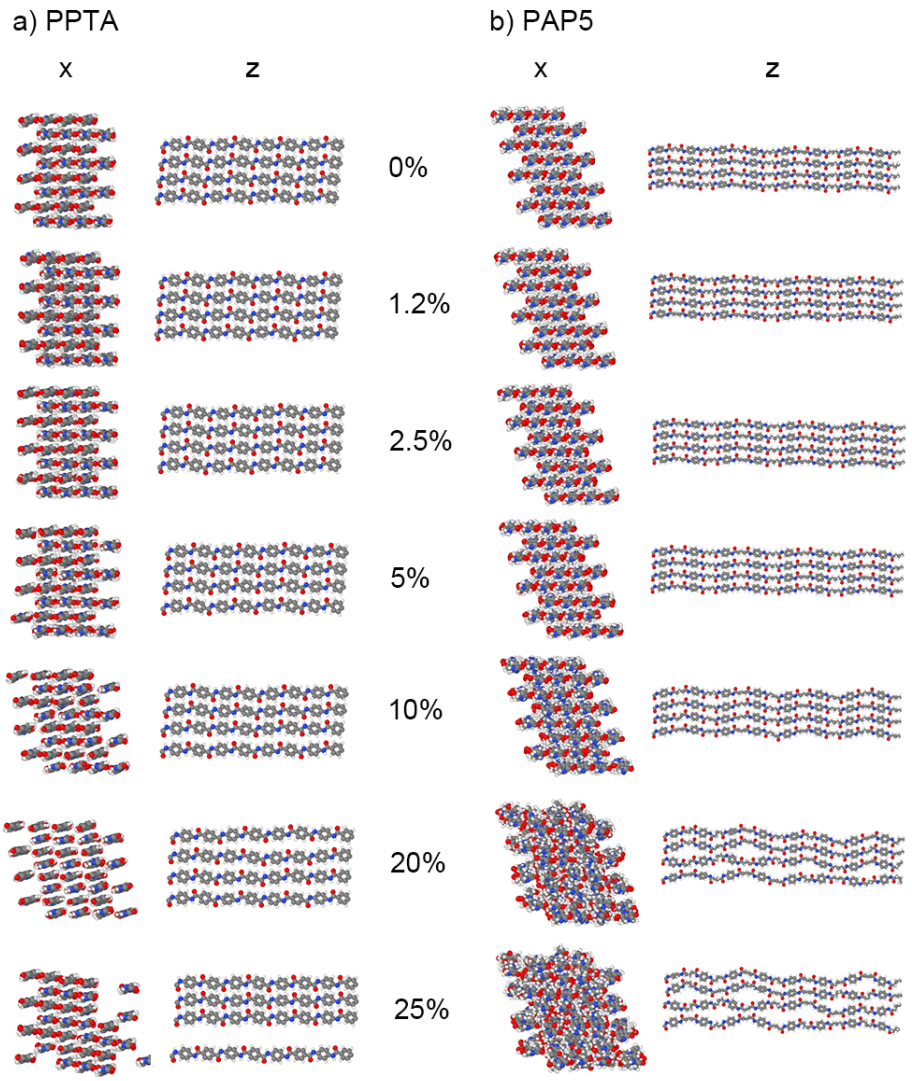

Figure 11: Snapshots of (a) PPTA and (b) PAP5 while strained in y-direction with a strain rate of 1×10^9 s^{-1} at 0, 5, 7.5, 10, 12.5 and 20% strains with the Liu force field as viewed from the x- and z-directions. Snapshots correspond to the solid circles on the stress-strain plots in Fig. 10.

with simulation snapshots in Fig. 13. The response of the polymers to strain in the z-direction is dominated by the π-stacking interactions between adjacent sheets. So, there is little change in the H-bonding RDFs with strain (Figs. 12c-f). In the π-stacking RDFs, the peak is observed to initially shift to the right (0-5% for PPTA and 0-10% strain for PAP5), corresponding to increasing distance between the sheets (Figs. 12g-j).

This trend continues until failure for PAP5. However, at about 8% strain, the PPTA

chains buckle at alternating amide linkages (Fig. 13a). This results in a split of the π-stacking peak for PPTA into two (Figs. 12h) since the buckling causes some aromatic rings to move closer together and others farther apart (Fig. S7). In contrast, the sheets move gradually apart until around 20% strain, at which point they separate in the middle leaving two groups of sheets with approximately equilibrium π-stacking distance (Fig. 13b and 12j). These different behaviors of PPTA and PAP5 in response to z-direction strain can be attributed to the better coplanarity of the PAP5 (Fig. S8), which corresponds to stronger intermolecular π-stacking interactions that enable it to resist buckling.

The Young's moduli in the z-direction of PPTA and PAP5 are the smallest among the three directions of strain (x, y and z) because π-stacking is weaker than covalent bonding (that resists strain in x) and H-bonding (that resists strain in y). In the z-direction, the stiffness of PAP5 (13 GPa) is slightly larger than that of PPTA (8 GPa). This high stiffness of PAP5 is explained by the fact that its aromatic rings are more coplanar (Fig. S8), which corresponds to stronger intermolecular π-stacking interactions and increases the modulus in the z-direction.

As seen in Figs. 12a-b, PAP5 exhibits a failure strain at 20%, but PPTA does not fail until 25% strain. This is because the buckling in PPTA accommodates some of the strain. In the π-stacking RDFs of PPTA (Figs. 12g-h), the average distance decreases with strain but the width of the peak dramatically increases, corresponding to the loss of π-π registry due to strain-induced buckling (Fig. 13a). This loss of π-π registry and lower coplanarity weakens the π-stacking interactions, which results in the smaller ultimate stress of PPTA (0.72 GPa) than that of PAP5 (0.99 GPa).

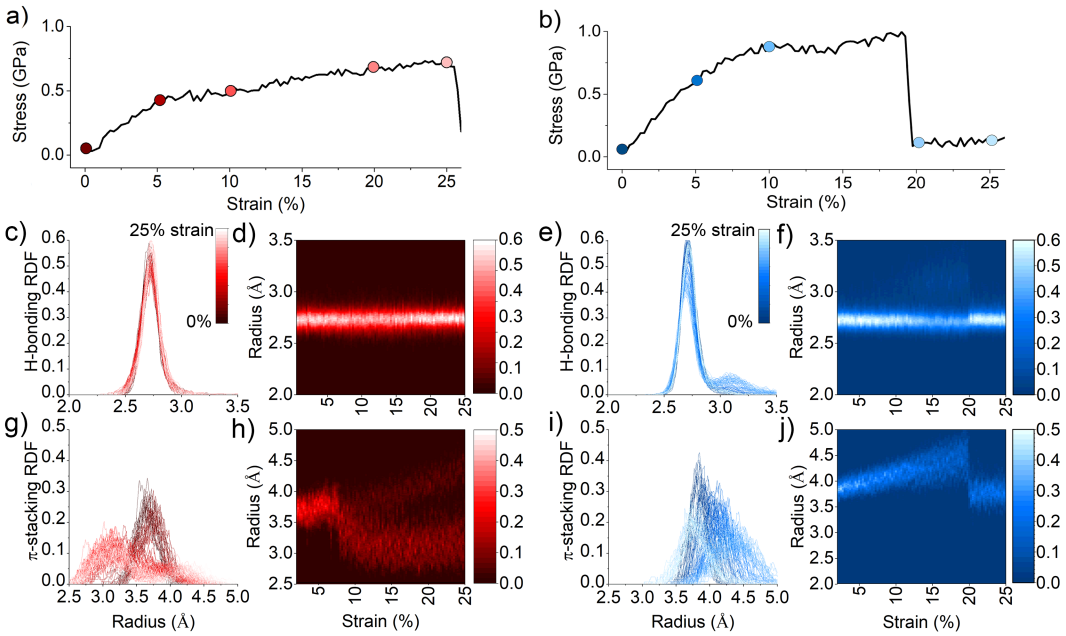

Figure 12: Stress-strain behavior (a and b) and RDF profiles and heat maps for H-bonding (c, d, e, and f) and π-stacking (g, h, i, and j) for PPTA (a, c, d, g, and h) and PAP5 (b, e, f, i, and j) strained in the z-direction with Liu force field. The RDFs are normalized by the number of bonds per unit cell. Movies showing the evolution of the stress and RDF distributions as well as the time evolution of the models are available in the Supplemental Information.

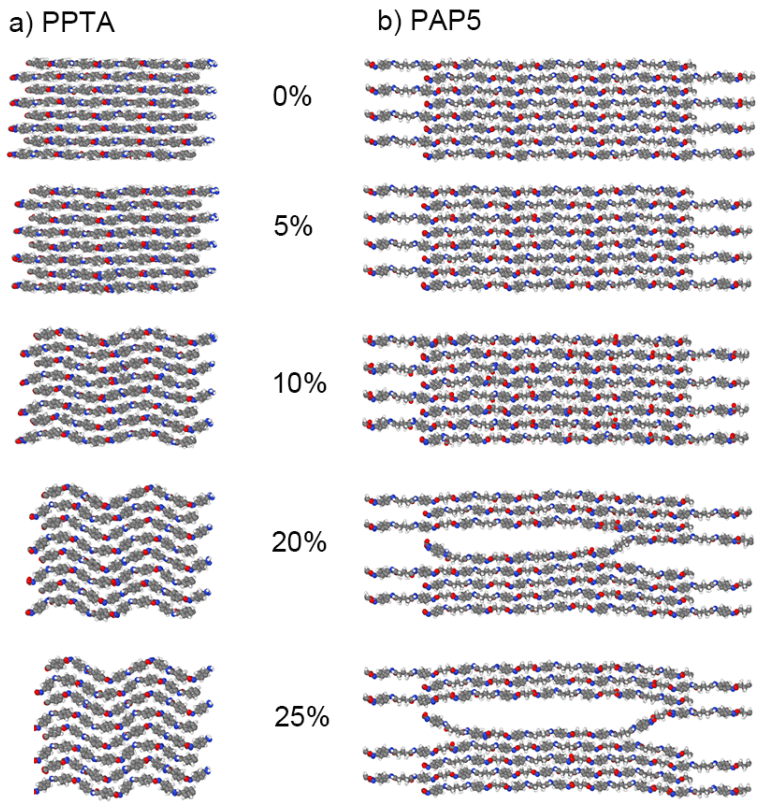

Figure 13: Snapshots of (a) PPTA and (b) PAP5 while strained in z-direction with a strain rate of 1×10^{9} s^{-1} at 0, 5, 7.5, 10, 12.5 and 20% strains with the Liu force field as viewed from the y-direction. Snapshots correspond to the solid circles on the stress-strain plots in Fig. 12.

Conclusions

Molecular dynamics simulations were used to study two polyamides, PPTA and PAP5. To ensure accurate modeling of these materials, seven different reactive and two non-reactive force fields were evaluated based on their ability to reproduce the unit cell lattice parameters of the polymer crystals as well as H-bonding and π-stacking distances within the crystal structure. Stress-strain simulations were performed with the force fields that were most accurate in terms of static properties. The results indicated that the ReaxFF force field developed by Liu was best for studying structure-property relationships of PPTA and PAP5. The mechanical properties of the two polymer crystals were calculated, compared to each other and, for PPTA, compared qualitatively to previously reported experimental data.

For strain in the chain-direction, it was found that the ultimate stress and failure strain of PAP5 were larger than those of PPTA, but the low-strain elastic modulus of PAP5 was smaller. These trends were investigated in terms of the waviness at different strains, as well as intramolecular amide and H-bond densities. One key difference between PPTA and PAP5 was found to be the initial (zero strain) conformation which was extended for PPTA and wavy for PAP5. The loose conformation of PAP5 gave it an additional degree of freedom that could accommodate low strain (up to about 4%) without stretching covalent bonds within the chains. This resulted in a smaller stiffness at low strains and a larger failure strain for PAP5 than PPTA. However, different mechanisms explained the high strain behavior leading to a larger high-strain stiffness and ultimate stress for PAP5 than PPTA. This difference was attributed to better alignment of PAP5 chains in the strained conformation.

Simulations of strain in the transverse directions demonstrated significant anisotropy of the mechanical properties, reflecting the anisotropic material structure. In both of the transverse directions, where intermolecular interactions (H-bonding and π-stacking) were dominant, the stiffness and ultimate stress of the crystals were much lower than those in the chain direction which were determined primarily by intramolecular interactions. The y-direction strain response was dominated by H-bonding between adjacent chains. The

stronger H-bonding of PPTA resulted in higher stiffness and larger ultimate strength than PAP5. Both crystals exhibited yield in response to strain in the y-direction. However, yielding of PPTA was due to inter-sheet slip and the yield strength was lower than that of PAP5 where yielding was associated with breaking of H-bond interactions. Strain in the z-direction was accommodated by π-stacking interactions. In this direction, PPTA had lower stiffness and ultimate stress than PAP5. This was explained by the coplanarity of the rings in PAP5 which resulted in stronger π-π interactions, as well as buckling of the PPTA chains in response to strain in the z-direction.

Overall, this study demonstrated the importance of force field selection for accurate modeling of polyamides. The force field evaluation also emphasized that models that accurately capture the commonly studied PPTA may not necessarily be suitable for polyamides generally. However, the fact that one of the force fields was suitable for both PPTA and PAP5 suggests that it may be suitable for other polyamides as well. Further, the comparison of PPTA to PAP5 reported here highlighted how small changes in the polymer structure, in this case substituting an aromatic linker for an aliphatic linker, can have dramatic effects on mechanical properties. Understanding the atomistic mechanisms underlying stress-strain behavior can enable identification of polymers with desired and potentially tunable properties for a variety of emerging applications.

Acknowledgement

We acknowledge ExxonMobil Research and Engineering Company for financial support of this work. The stimulating discussions with ExxonMobil colleagues (Ozcan Altintas, Arben Jusufi, Aruna Mohan, Agostino Pietrangelo, Thomas Sun, Pamela J Wright) are highly appreciated. The simulations were in part run using the Extreme Science and Engineering Discovery Environment (XSEDE), which is supported by National Science Foundation Grant ACI-1548562.

Supporting Information

Movies showing the evolution of the stress and RDF distributions as well as the time evolution of the PPTA and PAP5 strained in the x, y, and z-directions (Movies S1-6). Figures including comparison between step-wise stretching and continuous stretching approaches at four different strain rates (Figure S1); snapshots of PPTA strained in the z-direction before and after inter-chain slip occurs with the OPLS potential (Figure S2); snapshots of PPTA with the Liu and Vashisth potentials at 8% strain in the z-direction (Figure S3); lattice parameters and stress of PAP5 as functions of time during stretching and relaxation processes (Figure S4); stress and ring-ring angle of PPTA and PAP5 as functions of strain in the x-direction (Figure S5); inter-sheet slip, stress, and ring-ring angle of PPTA and PAP5 as functions of strain in y-direction (Figure S6); snapshots of ring pairs of PAP5 strained in z-direction at 25% (Figure S7); proximity and coplanarity RDFs of PPTA and PAP5 before stretching in the z-direction (Figure S8).

References

(1) Deshmukh, Y. S.; Wilsens, C. H.; Verhoef, R.; Hansen, M. R.; Dudenko, D.; Graf, R.; Klop, E. A.; Rastogi, S. Conformational and structural changes with increasing methylene segment length in aromatic–aliphatic polyamides. *Macromolecules* **2016**, *49*, 950–962.

(2) Dobb, M.; Johnson, D.; Saville, B. Supramolecular structure of a high-modulus polyaromatic fiber (Kevlar 49). *Journal of Polymer Science: Polymer Physics Edition* **1977**, *15*, 2201–2211.

(3) Shim, V.; Lim, C.; Foo, K. Dynamic mechanical properties of fabric armour. *International Journal of Impact Engineering* **2001**, *25*, 1–15.

(4) Yang, H. *Kevlar aramid fiber*; Wiley, 1993.

(5) Sockalingam, S.; Chowdhury, S. C.; Gillespie Jr, J. W.; Keefe, M. Recent advances in modeling and experiments of Kevlar ballistic fibrils, fibers, yarns and flexible woven textile fabrics–a review. *Textile Research Journal* **2017**, *87*, 984–1010.

(6) Kim, J.; McDonough, W. G.; Blair, W.; Holmes, G. A. The modified-single fiber test: A methodology for monitoring ballistic performance. *Journal of applied polymer science* **2008**, *108*, 876–886.

(7) Krishnan, K.; Sockalingam, S.; Bansal, S.; Rajan, S. Numerical simulation of ceramic composite armor subjected to ballistic impact. *Composites Part B: Engineering* **2010**, *41*, 583–593.

(8) Northolt, M. X-ray diffraction study of poly (p-phenylene terephthalamide) fibres. *European Polymer Journal* **1974**, *10*, 799–804.

(9) Mercer, B.; Zywicz, E.; Papadopoulos, P. Molecular dynamics modeling of PPTA crystallite mechanical properties in the presence of defects. *Polymer* **2017**, *114*, 329–347.

(10) Grujicic, M.; Ramaswami, S.; Snipes, J.; Yavari, R.; Lickfield, G.; Yen, C.-F.; Cheeseman, B. Molecular-level computational investigation of mechanical transverse behavior of p-phenylene terephthalamide (PPTA) fibers. *Multidiscipline Modeling in Materials and Structures* **2013**, *9*, 462–498.

(11) Lim, J.; Zheng, J. Q.; Masters, K.; Chen, W. W. Effects of gage length, loading rates, and damage on the strength of PPTA fibers. *International Journal of Impact Engineering* **2011**, *38*, 219–227.

(12) Rutledge, G.; Suter, U.; Papaspyrides, C. Analysis of structure of polymorphism in poly (p-phenyleneterephthalamide) through correlation of simulation and experiment. *Macromolecules* **1991**, *24*, 1934–1943.

(13) Greenwood, J.; Rose, P. Compressive behaviour of Kevlar 49 fibres and composites. *Journal of materials science* **1974**, *9*, 1809–1814.

(14) Dobb, M.; Johnson, D.; Saville, B. Compressional behaviour of Kevlar fibres. *Polymer* **1981**, *22*, 960–965.

(15) Singletary, J.; Davis, H.; Ramasubramanian, M.; Knoff, W.; Toney, M. The transverse compression of PPTA fibers Part I Single fiber transverse compression testing. *Journal of Materials Science* **2000**, *35*, 573–581.

(16) Cheng, M.; Chen, W.; Weerasooriya, T. Mechanical properties of Kevlar® KM2 single fiber. *J. Eng. Mater. Technol.* **2005**, *127*, 197–203.

(17) Rao, Y.; Waddon, A.; Farris, R. Structure–property relation in poly (p-phenylene terephthalamide)(PPTA) fibers. *Polymer* **2001**, *42*, 5937–5946.

(18) Prevorsek, D. C.; Kwon, Y. D.; Chin, H. B. Analysis of the temperature rise in the projectile and extended chain polyethylene fiber composite armor during ballistic impact and penetration. *Polymer Engineering & Science* **1994**, *34*, 141–152.

(19) Cline, J.; Wu, V.; Moy, P. *Assessment of the Tensile properties for single fibers*; 2018.

(20) Tashiro, K.; Kobayashi, M.; Tadokoro, H. Calculation of three-dimensional elastic constants of polymer crystals. 2. Application to orthorhombic polyethylene and poly (vinyl alcohol). *Macromolecules* **1978**, *11*, 914–918.

(21) Tashiro, K.; Kobayashi, M.; Tadokoro, H. Elastic moduli and molecular structures of several crystalline polymers, including aromatic polyamides. *Macromolecules* **1977**, *10*, 413–420.

(22) Mayo, S. L.; Olafson, B. D.; Goddard, W. A. DREIDING: a generic force field for molecular simulations. *Journal of Physical chemistry* **1990**, *94*, 8897–8909.

(23) Nimmanpipug, P.; Tashiro, K.; Rangsiman, O. Factors governing the three-dimensional hydrogen-bond network structure of poly (m-phenylene isophthalamide) and a series of its model compounds. 3. Energy terms indispensable to the crystal structure prediction. *The Journal of Physical Chemistry B* **2003**, *107*, 8343–8350.

(24) Sun, H. COMPASS: an ab initio force-field optimized for condensed-phase applications overview with details on alkane and benzene compounds. *The Journal of Physical Chemistry B* **1998**, *102*, 7338–7364.

(25) Grujicic, M.; Bell, W.; Glomski, P.; Pandurangan, B.; Yen, C.-F.; Cheeseman, B. Filament-level modeling of aramid-based high-performance structural materials. *Journal of materials engineering and performance* **2011**, *20*, 1401–1413.

(26) Van Duin, A. C.; Dasgupta, S.; Lorant, F.; Goddard, W. A. ReaxFF: a reactive force field for hydrocarbons. *The Journal of Physical Chemistry A* **2001**, *105*, 9396–9409.

(27) Yılmaz, D. E. Modeling failure mechanisms of poly (p-phenylene terephthalamide) fiber using reactive potentials. *Computational Materials Science* **2015**, *109*, 183–193.

(28) Budzien, J.; Thompson, A. P.; Zybin, S. V. Reactive molecular dynamics simulations of shock through a single crystal of pentaerythritol tetranitrate. *The Journal of Physical Chemistry B* **2009**, *113*, 13142–13151.

(29) Liu, L.; Liu, Y.; Zybin, S. V.; Sun, H.; Goddard III, W. A. ReaxFF-lg: Correction of the ReaxFF reactive force field for London dispersion, with applications to the equations of state for energetic materials. *The Journal of Physical Chemistry A* **2011**, *115*, 11016–11022.

(30) Mercer, B.; Zywicz, E.; Papadopoulos, P. A molecular dynamics-based analysis of the influence of strain-rate and temperature on the mechanical strength of PPTA crystallites. *Polymer* **2017**, *129*, 92–104.

(31) Chowdhury, S. C.; Sockalingam, S.; Gillespie, J. W. Molecular dynamics modeling of the effect of axial and transverse compression on the residual tensile properties of ballistic fiber. *Fibers* **2017**, *5*, 7.

(32) Nimmanpipug, P.; Tashiro, K.; Maeda, Y.; Rangsiman, O. Factors governing the three-dimensional hydrogen bond network structure of poly (m-phenylene isophthalamide) and a series of its model compounds:(1) Systematic classification of structures analyzed by the X-ray diffraction method. *The Journal of Physical Chemistry B* **2002**, *106*, 6842–6848.

(33) Lomicka, C.; Thomas, J.; LaBarre, E.; Trexler, M.; Merkle, A. *Dynamic Behavior of Materials, Volume 1*; Springer, 2014; pp 187–193.

(34) Chowdhury, S. C.; Gillespie Jr, J. W. A molecular dynamics study of the effects of hydrogen bonds on mechanical properties of Kevlar® crystal. *Computational Materials Science* **2018**, *148*, 286–300.

(35) Sun, H.; Mumby, S. J.; Maple, J. R.; Hagler, A. T. An ab initio CFF93 all-atom force field for polycarbonates. *Journal of the American Chemical Society* **1994**, *116*, 2978–2987.

(36) BIOVIA, BIOVIA Material Studio. 2020; `http://www.3ds.com/products-services/biovia/products/molecular-modeling-simulation/biovia-materials-studio`, Last accessed 16 February 2021.

(37) Northolt, M.; Van Aartsen, J. On the crystal and molecular structure of poly-(p-phenylene terephthalamide). *Journal of Polymer Science: Polymer Letters Edition* **1973**, *11*, 333–337.

(38) Dodda, L. S.; Cabeza de Vaca, I.; Tirado-Rives, J.; Jorgensen, W. L. LigParGen web server: an automatic OPLS-AA parameter generator for organic ligands. *Nucleic acids research* **2017**, *45*, W331–W336.

(39) Dauber-Osguthorpe, P.; Roberts, V. A.; Osguthorpe, D. J.; Wolff, J.; Genest, M.; Hagler, A. T. Structure and energetics of ligand binding to proteins: Escherichia coli dihydrofolate reductase-trimethoprim, a drug-receptor system. *Proteins: Structure, Function, and Bioinformatics* **1988**, *4*, 31–47.

(40) Zhang, L.; Duin, A. C. v.; Zybin, S. V.; Goddard, W. A. Thermal decomposition of hydrazines from reactive dynamics using the ReaxFF reactive force field. *The Journal of Physical Chemistry B* **2009**, *113*, 10770–10778.

(41) Kamat, A. M.; van Duin, A. C.; Yakovlev, A. Molecular dynamics simulations of laser-induced incandescence of soot using an extended ReaxFF reactive force field. *The Journal of Physical Chemistry A* **2010**, *114*, 12561–12572.

(42) Mattsson, T. R.; Lane, J. M. D.; Cochrane, K. R.; Desjarlais, M. P.; Thompson, A. P.; Pierce, F.; Grest, G. S. First-principles and classical molecular dynamics simulation of shocked polymers. *Physical Review B* **2010**, *81*, 054103.

(43) Wood, M. A.; Van Duin, A. C.; Strachan, A. Coupled thermal and electromagnetic induced decomposition in the molecular explosive αHMX; a reactive molecular dynamics study. *The Journal of Physical Chemistry A* **2014**, *118*, 885–895.

(44) Vashisth, A.; Ashraf, C.; Zhang, W.; Bakis, C. E.; Van Duin, A. C. Accelerated ReaxFF simulations for describing the reactive cross-linking of polymers. *The Journal of Physical Chemistry A* **2018**, *122*, 6633–6642.

(45) Plimpton, S. Fast parallel algorithms for short-range molecular dynamics. *Journal of computational physics* **1995**, *117*, 1–19.

(46) Stukowski, A. Visualization and analysis of atomistic simulation data with OVITO–the Open Visualization Tool. *Modelling and Simulation in Materials Science and Engineering* **2009**, *18*, 015012.

(47) Hoover, W. G. Canonical dynamics: Equilibrium phase-space distributions. *Physical review A* **1985**, *31*, 1695.

(48) Hoover, W. G. Constant-pressure equations of motion. *Physical Review A* **1986**, *34*, 2499.

(49) Wu, X.; Moon, R. J.; Martini, A. Tensile strength of Iβ crystalline cellulose predicted by molecular dynamics simulation. *Cellulose* **2014**, *21*, 2233–2245.

(50) Dri, F. L.; Wu, X.; Moon, R. J.; Martini, A.; Zavattieri, P. D. Evaluation of reactive force fields for prediction of the thermo-mechanical properties of cellulose Iβ. *Computational Materials Science* **2015**, *109*, 330–340.

(51) Wu, X.; Moon, R. J.; Martini, A. Crystalline cellulose elastic modulus predicted by atomistic models of uniform deformation and nanoscale indentation. *Cellulose* **2013**, *20*, 43–55.

(52) Yu, R.; Zhai, P.; Li, G.; Liu, L. Molecular dynamics simulation of the mechanical properties of single-crystal bulk Mg 2 Si. *Journal of electronic materials* **2012**, *41*, 1465–1469.

(53) Yang, X.; Zhou, T.; Chen, C. Effective elastic modulus and atomic stress concentration of single crystal nano-plate with void. *Computational materials science* **2007**, *40*, 51–56.

(54) Tschopp, M. A. Uniaxial Tension. 2020; `https://icme.hpc.msstate.edu/mediawiki/index.php/Uniaxial_Tension.html`, Last accessed 19 February 2021.

(55) Yilmaz, D. E.; van Duin, A. C. Investigating structure property relations of poly (p-phenylene terephthalamide) fibers via reactive molecular dynamics simulations. *Polymer* **2018**, *154*, 172–181.

(56) Chenoweth, K.; Van Duin, A. C.; Goddard, W. A. ReaxFF reactive force field for molecular dynamics simulations of hydrocarbon oxidation. *The Journal of Physical Chemistry A* **2008**, *112*, 1040–1053.

(57) Cheng, M.; Chen, W.; Weerasooriya, T. Experimental investigation of the transverse mechanical properties of a single Kevlar® KM2 fiber. *International Journal of Solids and Structures* **2004**, *41*, 6215–6232.

(58) Rao, Y.; Waddon, A.; Farris, R. The evolution of structure and properties in poly (p-phenylene terephthalamide) fibers. *Polymer* **2001**, *42*, 5925–5935.

(59) Zhu, D.; Mobasher, B.; Rajan, S. D. Dynamic tensile testing of Kevlar 49 fabrics. *Journal of materials in civil engineering* **2011**, *23*, 230–239.

(60) Thomas, J. A.; Shanaman, M. T.; Lomicka, C. L.; Boyle, M. P.; Calderon-Colon, X.; LaBarre, E. D.; Tiffany, J. E.; Trexler, M. M. Multiscale modeling of high-strength fibers and fabrics. Micro-and Nanotechnology Sensors, Systems, and Applications IV. 2012; p 83731S.

(61) Wang, Y.; Xia, Y. The effects of strain rate on the mechanical behaviour of kevlar fibre bundles: an experimental and theoretical study. *Composites Part A: Applied Science and Manufacturing* **1998**, *29*, 1411–1415.

(62) Wang, Y.; Xia, Y. Experimental and theoretical study on the strain rate and temperature dependence of mechanical behaviour of Kevlar fibre. *Composites Part A: Applied Science and Manufacturing* **1999**, *30*, 1251–1257.

(63) Rutledge, G.; Suter, U. Calculation of Mechanical Properties of Poly (p-phenylene terephthalamide) by Atomistic Modelling. *Polymer* **1991**, *32*, 2179–2189.

(64) Sakurada, I.; Kaji, K. Relation between the polymer conformation and the elastic mod-

ulus of the crystalline region of polymer. Journal of Polymer Science Part C: Polymer Symposia. 1970; pp 57–76.

(65) Li, Y.; Goddard, W. A. Nylon 6 crystal structures, folds, and lamellae from theory. *Macromolecules* **2002**, *35*, 8440–8455.

(66) Tasaki, M.; Yamamoto, H.; Yoshioka, T.; Hanesaka, M.; Ninh, T. H.; Tashiro, K.; Jeon, H. J.; Choi, K. B.; Jeong, H. S.; Song, H. H., et al. Microscopically-viewed relationship between the chain conformation and ultimate Young's modulus of a series of arylate polyesters with long methylene segments. *Polymer* **2014**, *55*, 1799–1808.

(67) Hollars, C. W.; Lane, S. M.; Huser, T. Controlled non-classical photon emission from single conjugated polymer molecules. *Chemical physics letters* **2003**, *370*, 393–398.

(68) Prime, R. B.; Wunderlich, B.; Melillo, L. Extended-chain crystals. V. Thermal analysis and electron microscopy of the melting process in polyethylene. *Journal of Polymer Science Part A-2: Polymer Physics* **1969**, *7*, 2091–2097.

(69) Wu, Q.; Xue, Z.; Qi, Z.; Wang, F. Synthesis and characterization of PAn/clay nanocomposite with extended chain conformation of polyaniline. *Polymer* **2000**, *41*, 2029–2032.

(70) Morgan, P. Synthesis and properties of aromatic and extended chain polyamides. *Macromolecules* **1977**, *10*, 1381–1390.

(71) Wang, Z.-Y.; Yao, Z.-F.; Lu, Y.; Ding, L.; Yu, Z.-D.; You, H.-Y.; Wang, X.-Y.; Zhou, Y.-Y.; Zou, L.; Wang, J.-Y., et al. Precise tracking and modulating aggregation structures of conjugated copolymers in solutions. *Polymer Chemistry* **2020**, *11*, 3716–3722.

(72) Ullner, M.; Woodward, C. E. Orientational correlation function and persistence lengths of flexible polyelectrolytes. *Macromolecules* **2002**, *35*, 1437–1445.

(73) Niu, Y.; Hou, H.; Zhu, Y. Self-assembly of d 10 metal adduct polymers bridged by bipyridyl-based ligands. *Journal of Cluster Science* **2003**, *14*, 483–493.

(74) Jin, C.-M.; Chen, Z.-F.; Mei, H.-F.; Shi, X.-K. Ag (I) coordination polymers with flexible bis-imidazole ligands: 2D interwoven structure and wavy layer network based on silver–silver interactions. *Journal of Molecular Structure* **2009**, *921*, 58–62.

(75) Miyake, H.; Gotoh, Y.; Ohkoshi, Y.; Nagura, M. Molecular weight dependence of tensile properties in poly (vinyl alcohol) fibers. *Polymer journal* **2000**, *32*, 1049–1051.

(76) Lotz, B. Original Crystal Structures of Even–Even Polyamides Made of Pleated and Rippled Sheets. *Macromolecules* **2021**, *54*, 551–564.

(77) Nishino, T.; Takano, K.; Nakamae, K. Elastic modulus of the crystalline regions of cellulose polymorphs. *Journal of Polymer Science Part B: Polymer Physics* **1995**, *33*, 1647–1651.

(78) Hansen, M. R.; Graf, R.; Spiess, H. W. Solid-state NMR in macromolecular systems: insights on how molecular entities move. *Accounts of chemical research* **2013**, *46*, 1996–2007.

(79) Tashiro, K.; Kobayashi, M. Theoretical evaluation of three-dimensional elastic constants of native and regenerated celluloses: role of hydrogen bonds. *Polymer* **1991**, *32*, 1516–1526.

(80) Feng, W.; Zou, G.; Ding, Y.; Ai, T.; Wang, P.; Ren, Z.; Ji, J. Effect of Aliphatic Diacid Chain Length on Properties of Semiaromatic Copolyamides Based on PA10T and Their Theoretical Study. *Industrial & Engineering Chemistry Research* **2019**, *58*, 7217–7226.

(81) Young, R.; Lu, D.; Day, R.; Knoff, W.; Davis, H. Relationship between structure and mechanical properties for aramid fibres. *Journal of materials science* **1992**, *27*, 5431–5440.

(82) Mercer, B. S. Molecular Dynamics Modeling of PPTA Crystals in Aramid Fibers. Ph.D. thesis, UC Berkeley, 2016.

(83) Hearle, J. W.; Morton, W. E. *Physical properties of textile fibres*; Woodhead Publishing Limited: Cambridge, 2008.

Graphical TOC Entry